Solar Phys (2007) 244: 95–114
DOI 10.1007/s11207-007-9002-x

How Does Large Flaring Activity from the Same Active Region Produce Oppositely Directed Magnetic Clouds?

Louise K. Harra · Nancy U. Crooker · Cristina H. Mandrini · Lidia van Driel-Gesztelyi · Sergio Dasso · Jingxiu Wang · Heather Elliott · Gemma Attrill · Bernard V. Jackson · Mario M. Bisi

Received: 22 January 2007 / Accepted: 9 July 2007 / Published online: 24 August 2007

Abstract We describe the interplanetary coronal mass ejections (ICMEs) that occurred as a result of a series of solar flares and eruptions from 4 to 8 November 2004. Two ICMEs/magnetic clouds occurring from these events had opposite magnetic orientations. This was despite the fact that the major flares related to these events occurred within the same active region that maintained the same magnetic configuration. The solar events in-

L.K. Harra (✉) · L. van Driel-Gesztelyi · G. Attrill
Mullard Space Science Laboratory, University College London, Holmbury St. Mary, Dorking, Surrey, RH5 6NT, UK
e-mail: lkh@mssl.ucl.ac.uk

N.U. Crooker
Center for Space Physics, Boston University, Boston, MA, USA

C.H. Mandrini · S. Dasso
Instituto de Astronomía y Física del Espacio, CONICET-UBA, CC. 67, Suc. 28, 1428 Buenos Aires, Argentina

L. van Driel-Gesztelyi
Observatoire de Paris, LESIA, FRE 2461 (CNRS), 92195 Meudon Principal Cedex, France

L. van Driel-Gesztelyi
Konkoly Observatory of the Hungarian Academy of Sciences, Budapest, Hungary

J. Wang
National Astronomical Observatory, Chinese Academy of Sciences, Beijing, China

S. Dasso
Departamento de Física, Facultad de Ciencias Exactas y Naturales, Universidad de Buenos Aires, 1428 Buenos Aires, Argentina

H. Elliott
Southwest Research Institute, 6220 Culebra Road, San Antonio, TX 78238, USA

B.V. Jackson · M.M. Bisi
Center for Astrophysics and Space Sciences, University of California, San Diego, La Jolla, CA, USA

clude a wide array of activities: flares, trans-equatorial coronal loop disappearance and reformation, trans-equatorial filament eruption, and coronal hole interaction. The first major ICME/magnetic cloud was predominantly related to the active region 10696 eruption. The second major ICME/magnetic cloud was found to be consistent with the magnetic orientation of an erupting trans-equatorial filament or else a rotation of 160° of a flux rope in the active region. We discuss these possibilities and emphasize the importance of understanding the magnetic evolution of the solar source region before we can begin to predict geoeffective events with any accuracy.

1. Introduction

The source regions of geomagnetic storms have long been sought after. The most likely solar events to be geoeffective are those from fast full halo coronal mass ejections (CMEs) that are also associated with large flares occurring close to the central meridian. These will naturally bring the strongest magnetic fields to the magnetosphere and, hence, have the potential (magnetic field direction permitting) to produce large geomagnetic storms (*e.g.*, Srivastava and Venkatakrishnan, 2004). A strong link has been established between the magnetic configuration of eruptive filaments and magnetic clouds (*e.g.*, Marubashi, 1986; Bothmer and Rust, 1997). However, the link between active regions (ARs) and geoeffective events is less clear. Pevtsov and Canfield (2001) studied the special case of S-shaped sigmoidal structures. They found that there was a tendency for sigmoids with southward-directed magnetic fields to be associated with stronger geomagnetic storms, whereas the northward-directed sigmoids tend to be associated with weaker geomagnetic effects. Many papers have concentrated on statistical studies like these. Recent work by Liu, Webb, and Zhao (2006) have taken a different approach and studied the flaring evolution of three ARs to determine whether it is possible for eruptions from a region with a particular magnetic field orientation to always be geoeffective. They found that, although it is often seen that the same AR may produce multiple halo CMEs, not all of these will have the same geoeffectiveness. To know how geoeffective the storm will be one must know which component of the complex AR actually erupted.

It is also well known that CMEs are large-scale phenomena. Recently, there has been interest in the relationship between trans-equatorial loops (TELs) and CMEs. Khan and Hudson (2000) studied a series of homologous eruptions of TELs and demonstrated that they constituted at least part of the subsequent CME. The well-studied Bastille Day event in 2000 was shown to have a trans-equatorial (TE) filament eruption entangled in the erupted material (Wang *et al.*, 2006a, 2006b). The TE filament erupted before the large AR flare took place, and formed part of the CME material. A statistical survey of nearly 300 Earth-directed CMEs was carried out by Zhou, Wang, and Zhang (2006) to ascertain how large-scale magnetic structures are related to CMEs. They categorized these structures into four types, which included TELs and TE filaments. Trans-equatorial loops were found to erupt in 40% of the CMEs, and TE filaments were found to erupt in 13% of the cases. The large-scale structures are clearly of great importance when trying to understand CMEs. Wang *et al.* (2007) discuss the evolution of TE activity during the events of November 2004.

A subset of interplanetary coronal mass ejections (ICMEs) are known as magnetic clouds (MCs). This special case was defined by Burlaga (1995) as having strong magnetic fields (when compared with the surroundings), displaying a large and coherent rotation and a depressed ion temperature. Detailed case studies have shown that the magnetic field orientation and the direction of the polarity inversion line (or observed prominence) in the source region of a CME are consistent with the magnetic field orientation and axis of the cloud, by

the time the cloud reaches the Earth (*e.g.*, McAllister *et al.*, 2001; Mandrini *et al.*, 2005; Fazakerley *et al.*, 2005). However, in the case study of the 12/14 May 1997 CME and cloud, a significant difference was found between the magnetic orientations of the source region and the MC. The latter could be caused by the rotation of the erupting filament, presumably resulting from the onset of a kink instability during its eruption (Webb *et al.*, 2000; Attrill *et al.*, 2006).

Much of the work carried out to date on the Sun – Earth connection has either looked at specific events in detail or else studied ICME/MCs on a statistical basis. We wish to investigate how the global magnetic evolution in the Sun will affect the orientation of the MCs that originate from the large flares and ejections from the same AR magnetic configuration. It has been suggested through a statistical study by Kang *et al.* (2006) that the field direction of MCs is reasonably well preserved as they travel through the heliosphere, making it possible to link them to the source regions. We therefore concentrate on two MCs that occurred during the well-known active period of November 2004.

On 1 November 2004 a new active region (AR10696) appeared close to the east limb in the northern hemisphere. This region continued to grow in size and complexity, producing large (in X-ray classification) solar flares. By 6 November the GOES X-ray level reached close to the X level, and on 7 November there was an X2 class flare (see Figure 1). A weaker β-type active region (AR10695) was on the opposite (southern) hemisphere to the west of AR10696. Chertok (2006) examined the EUV dimming in particular for this series of events. He found that there were homologous dimmings. There was a recurrent dimming region to the north of AR10696 between two coronal holes and also a TE dimming between AR10696 and AR10695. It may not be surprising that this is the case since the magnetic field orientation of the ARs appeared to stay the same during this period.

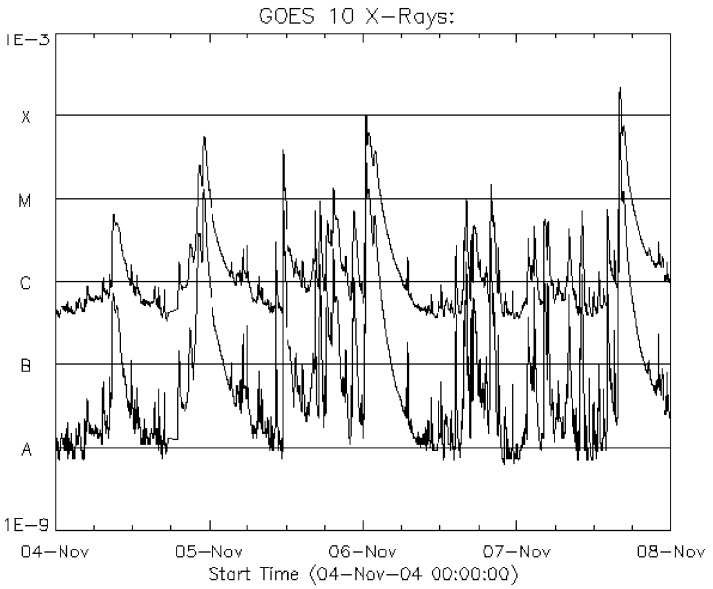

Figure 1 The GOES lightcurve from 4 November to the beginning of 8 November. As can be seen the flare magnitude increases to X class on 7 November. The flares related to the ICMEs studied in this paper are marked.

In this paper we investigate the large-scale magnetic connections between these two ARs and how these affect the interplanetary events that are observed at Earth. We look for the source regions of two ICME/magnetic clouds that produced major geomagnetic storms at Earth. In spite of the flaring site being the same, the magnetic orientation of the clouds are opposite. We explore the reasons for this.

2. Instrument Description

The data sets that we analyzed were predominantly from the Extreme Ultraviolet Imaging Telescope (SOHO-EIT, Delaboudinière *et al.*, 1995), the Michelson Doppler Imager (SOHO-MDI, Scherrer *et al.*, 1995), the Hα Telescope for Argentina (HASTA, Fernández Borda *et al.*, 2002), and the Solar Wind Electron Proton Alpha Monitor (SWEPAM, McComas *et al.*, 1998) and Magnetic Fields Experiment (Smith *et al.*, 1998) aboard the *Advance Composition Explorer* (ACE, Stone *et al.*, 1998).

The SOHO-EIT observations are full-Sun images in four different filters, with a pixel size of 2.6″. We mainly analyzed the observations made with the 195 Å filter.

The SOHO-MDI images the Sun on a 1024 × 1024 CCD camera through a series of increasingly narrow filters. The final elements, a pair of tunable Michelson interferometers, enable MDI to record filtergrams with a full width at half maximum (FWHM) bandwidth of 100 mÅ. In this paper we analyze 5-minute-averaged magnetograms of the full disk with a 96-minute cadence and a pixel size of 1.98″.

HASTA provides images in the hydrogen Hα emission line at 6563 Å. It uses a Lyot filter with a FWHM of 0.3 Å and has a pixel size of 2.07″.

The SWEPAM experiment provides measurements of electron and ion distribution functions in three dimensions over all of the velocity space needed to characterize the bulk flow and kinetic properties of the MCs analyzed here.

3. The Development of AR10696 and Its Linkage to AR10695

AR10696 was observed on 1 November 2004 as a new active region close to the east limb. By 3 November the flares were reaching M class with the region growing in size and complexity. It carried predominantly negative helicity (Williams *et al.*, 2005) and developed a curved inversion line aligned in the E – W direction. By 7 November the inversion line of the AR appeared to form a switchback with a TE filament toward the SW – S of the AR. Figure 1 shows the flaring activity that occurred from the start of 4 November. Except for an M flare on 4 November that occurred in AR10691, all large flares seen in GOES originated from AR10696 during this period.

When AR10696 first appeared on the disk there was no connection with the southern AR10695. As AR10696 rapidly evolved, a weak connection appeared on 2 and 3 November, and by 4 November bright TELs were seen, as illustrated in Figure 2. The TELs at this stage appear to be linking negative field in the northern AR to positive magnetic field in the southerly AR, which gives the TELs a northerly magnetic field direction. AR10695, in the south, was present during this rotation and had emerged within a positive coronal hole. A TE filament developed early on 7 November between these two ARs.

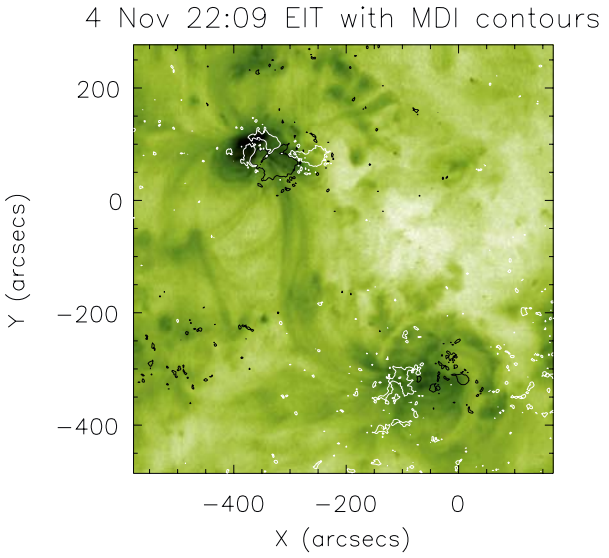

Figure 2 An EIT 195 Å image illustrating the connection between AR10696 (in the north) and AR10695 (in the south). A superposed MDI image shows black contours of negative magnetic field and white contours of positive magnetic field at 100-G intervals.

4. Shock – ICME – CME Associations

A series of large CMEs occurred during the time period of the flares in Figure 1, from 4 to 8 November. These are listed in row g of Table 1 along with the associated flares in row o. The flares all occurred in AR 10696, which is the region located to the north in Figure 2. Although other flares and CMEs occurred during this period, as seen in Figure 1, we have concentrated on the flares that are associated with the CMEs that have the largest angular extent and fastest speeds as observed by the Large Angle and Spectroscopic Coronagraph (SOHO-LASCO). From statistical studies these are the most likely events to be associated with geomagnetic storms (see, *e.g.*, Webb *et al.*, 2000; Vilmer *et al.*, 2003; Yashiro *et al.*, 2005). To determine the source regions of the ICMEs, we use several models in this section to determine which CME and flare was associated with each ICME.

4.1. Linking Shocks and ICMEs to CME Events

The interplanetary data from the ACE spacecraft at 1 AU during this period are shown in Figure 3. Red vertical lines in the second panel (proton speed, V_p) mark six forward shocks, labeled sequentially from 1 to 6. Their times are given in row b of Table 1. The third panel of Figure 3 indicates passage of three ICMEs labeled A, B, and C. In this panel, the black trace marking the measured proton temperature (T_p) falls below the red trace marking the expected temperature calculated from V_p (Elliott *et al.*, 2005). The times of the ICME boundaries are listed in rows k and l of Table 1. ICME A and ICME B both contain magnetic clouds, marked by blue horizontal lines running through the smooth magnetic field rotations labeled a and b in the plot of field latitude angle (θ_{GSE}) in the fourth panel and the longitude angle (ϕ_{GSE}) in the fifth panel. The times of the cloud boundaries are listed in rows m and n of Table 1. In both cases the clouds lie in the leading portion of the ICME and occupy only a fraction of the total volume, as commonly found (*e.g.*, Crooker *et al.*, 1998).

Table 1 attempts to associate shocks 1 – 6 and ICMEs A – C with halo or near-halo CMEs from the LASCO catalogue (http://cdaw.gsfc.nasa.gov/CME_list/). The times of their appearances in the C2 field of view are listed in row g. Four different predictive schemes are used.

Table 1 Predictive parameters for associating shocks and ICMEs with CMEs.

a	Forward shock	1	2	3	4	5		6	
b	Arrival at ACE	7 Nov 02:00	7 Nov 10:00	7 Nov 17:55	9 Nov 09:15	9 Nov 18:20		11 Nov 16:40	
c	Max ICME speed	700? km s^{-1}	700? km s^{-1}	720 km s^{-1}	790/820 km s^{-1}	820 km s^{-1}		675 km s^{-1}	
d	Cliver shock dep.	5 Nov 06:40	5 Nov 14:40	5 Nov 23:40	7 Nov 18:35/19:55	8 Nov 05:00		9 Nov 19:50	
e	STOA shock arr.	6 Nov 19:25		8 Nov 05:43	9 Nov 07:21			10 Nov 22:31	
f	HAFv.2 shock arr.	6 Nov 09:00,12:00		7 Nov 13:00	9 Nov 05:00			11 Nov 05:00	
g	CME seen in C2	4 Nov 23:30		6 Nov (01:32) 02:06	7 Nov 16:54		8 Nov 03:54	9 Nov 17:26	10 Nov 02:26
h	CME POS speed	1055 km s^{-1}		(818)1111 km s^{-1}	1759 km s^{-1}		462 km s^{-1}	2000 km s^{-1}	3387 km s^{-1}
i	Gopal. ICME arr.	7 Nov 08:35		8 Nov 07:30	8 Nov 22:45		12 Nov 09:25	10 Nov 17:55	10 Nov 16:15
j	Associated ICME	None		A	B	B	C		
k	ICME start time			7 Nov 22:30	9 Nov 20:25		12 Nov 05:20		
l	ICME stop time			9 Nov 09:15	11 Nov 18:45		13 Nov 21:35		
m	Cloud start time			7 Nov 22:30	9 Nov 20:30		None		
n	Cloud stop time			8 Nov 17:00	10 Nov 10:00				
o	Flare class	M5.5		(M9.3/M5.9)M3.6	X2				

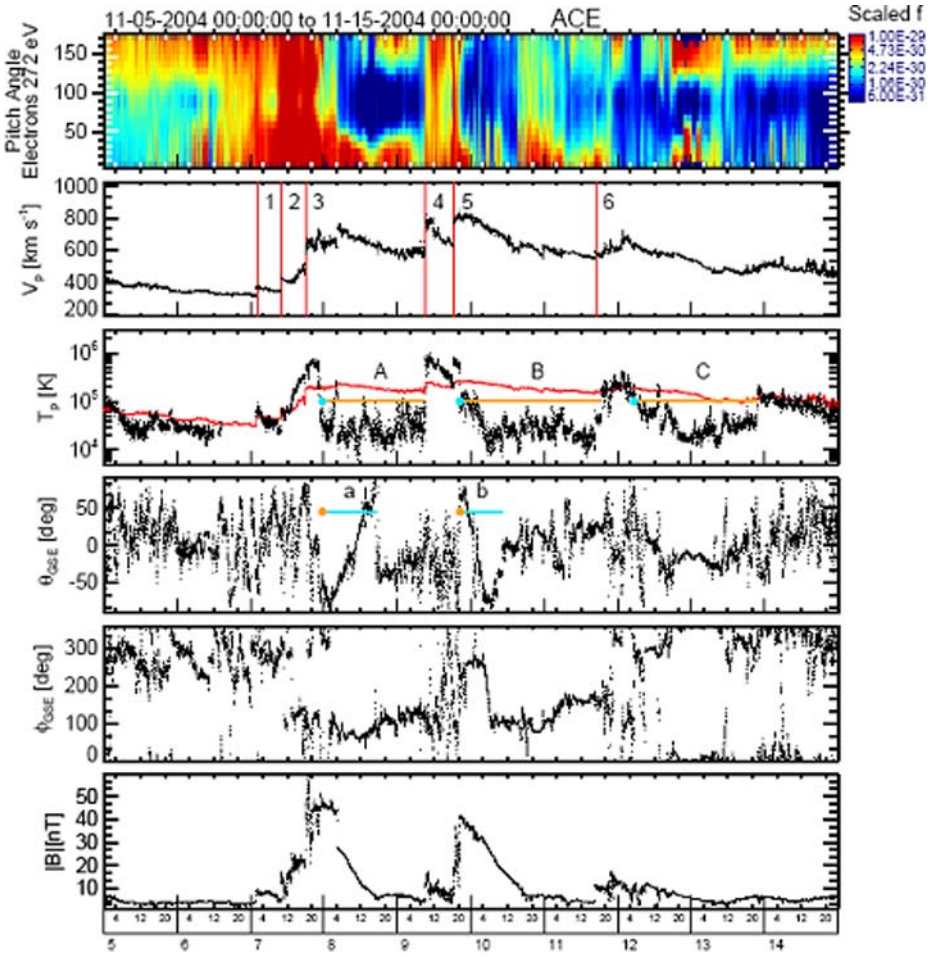

Figure 3 Time variations of suprathermal electron pitch-angle distributions, proton speed V_p and temperature T_p, magnetic field latitude (θ_{GSE}) and longitude (ϕ_{GSE}) angles in the Geocentric Solar Ecliptic (GSE) coordinates, and magnetic field magnitude (B) for a period of 10 days covering the passage of six forward shocks (marked in the V_p panel) and three ICMEs (marked in the T_p panel). The first two ICMEs contained MCs (marked in the θ_{GSE} panel).

Row d gives the time of CME/shock departure from the Sun calculated from the Cliver, Feynman, and Garrett (1990) empirical formula, which relates the maximum speed (row c) within an ICME observed at 1 AU to the average transit speed of its shock. These predicted departures are compared with the observed CME departures in row g. Rows e and f give the times of shock arrival at 1 AU predicted in the "Fearless Forecast" published on the Web at http://www.gi.alaska.edu/pipermail/gse-ff/. These predictions are made with two physics-based models, STOA (Shock-Time-of-Arrival model) and HAFv.2 (version 2 of the Hakamada – Akasofu – Fry model) (*e.g.*, Fry *et al.*, 2003). Row i gives the time of arrival of the ICME calculated from the Gopalswamy *et al.* (2001) empirical formula, which relates the measured plane-of-sky speed (POS) (row h) to the transit time to 1 AU. These predicted arrivals are to be compared with the observed ICME start times in row k.

The prediction results in Table 1 indicate relatively clear associations for the three ICMEs, as follows: ICME A with shock 3 and the 6 November 02:06 UT CME, ICME B with shock 4 and the 7 November 16:54 UT CME, and ICME C with the 8 November 03:54 UT CME. For ICME A, an earlier (01:32 UT) halo CME is also listed in row g. It was associated with two flares, noted in row o and discussed in Section 5.1.1; but presumably it was swept up by the faster CME at 02:06 UT, associated with an additional flare. In Figure 3, the smooth excursion in the magnetic latitude angle θ_{GSE} in the sheath preceding ICME A/cloud a may be a signature of that earlier CME. For ICME B, although the calculated departure and shock arrival times are in agreement with the event times, the calculated arrival time based on the CME projected speed is too early by nearly a day. A likely reason for this, discussed further in Section 5.2.1, is that the listed speed applies to a portion of the CME that appears to expand northward in the LASCO field of view rather than toward the Earth. The two calculated shock departure times are based upon two maxima in the in situ speed profile in row c, one following shock 4 and another following shock 5, which also precedes ICME B. Both shock 4 and shock 5 are thought to be driven by ICME B, even though the calculated departure of shock 5 does not match the observed arrival time. Apparently the two shocks reflect an interacting two-part structure, as discussed in Section 5.2.3. For ICME C there is no associated shock, consistent with the low projected CME speed (462 km s^{-1}). The calculated ICME arrival time (row i) from the 8 November 03:54 UT CME matches the observed arrival time to within ≈4 hours. Although shock 6 precedes ICME C, the calculated departure time in row d associates it with an earlier halo CME, on 9 November at 17:26 UT, from which the associated ICME presumably did not intercept Earth. Interception of a shock without a subsequent ICME is commonly interpreted in terms of the much larger expanse of shock fronts compared to ICME volumes.

The 4 November 23:30 UT CME associated with shock 1 and the 10 November 02:26 UT CME in the last column of Table 1 also apparently did not intercept Earth. It is somewhat surprising that none of the shocks can be traced back to the latter one, which has a remarkably high POS speed (3 387 km s^{-1}). For shocks 1 and 2, with no associated ICME interceptions, the calculated departure times in row d are based upon an assumed ICME speed of 700 km s^{-1}. The results, combined with those from the STOA and HAFv.2 models, suggest that shock 1 was driven by the 4 November 23:30 UT CME. Of the six shocks, this leaves only shock two without an associated source.

Figure 4 is a scatter plot that compares observed and predicted arrival times for the four shocks in Table 1 for which results from the physics-based models are available. To facilitate comparison, adjustments were required for the two empirical models. For the Cliver, Feynman, and Garrett (1990) formula for shock departure from the Sun, the predicted transit time was calculated and added to the time the CME left the Sun to obtain an arrival time. For the Gopalswamy *et al.* (2001) formula for ICME arrival, a transit time for passing through the sheath, from the shock to the ICME, was subtracted from the predicted time. For the two cases (shocks 1 and 4) with no ICME interception, minimal sheath transit times of 5 hours were assumed. Where two predictions are given in Table 1, for the HAFv.2 model in the case of shock 1 and for the Cliver, Feynman, and Garrett (1990) formula in the case of shock 4, those that agreed best with the observed times were selected for the plot.

The comparisons in Figure 4 show for the first time that the best associations can be made with the Cliver *et al.* formula. This seems reasonable since it is based upon an in situ speed that already reflects the effects of the interplanetary medium through which the ICME propagated. However, of the four models, the Cliver *et al.* formula is the only one that cannot predict in a forward sense; that is, it cannot be used to predict the arrival of a disturbance from solar parameters. A comparison between the predicted arrival times from the two physics-based models does not favor one over the other, at least for these few cases, even though the

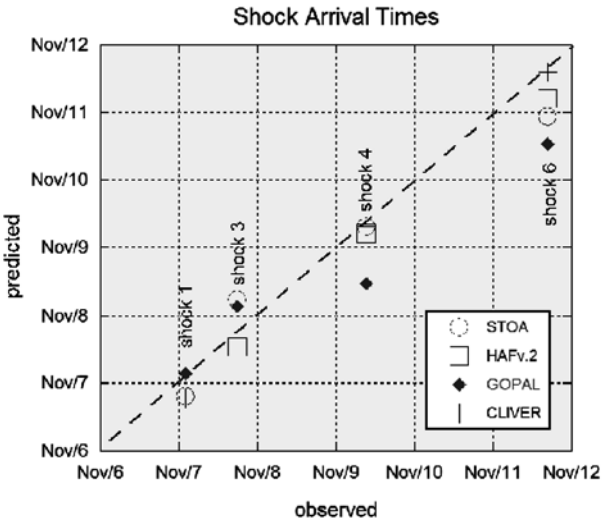

Figure 4 Comparison of predicted and observed shock arrival times for four different models. Predicted times are derived from parameters in Table 1.

HAFv.2 model has a realistic interplanetary medium based upon solar magnetic boundary conditions (see Fry *et al.*, 2003, for further comparisons). Overall the Gopalswamy *et al.* formula gives the poorest predictions, even though it gives the best prediction for shock 1. Other empirical formulas are available that might provide better matches (*e.g.*, Vrsnak and Gopalswamy, 2003; Schwenn *et al.*, 2005; Manoharan, 2006), but further comparisons are beyond the scope of this paper. Figure 4 accomplishes its purpose of demonstrating that the associations in Table 1 seem convincing. For further details on the Sun – Earth propagation speed of ICME B see Pohjolainen *et al.* (2007).

5. The Shock – ICME – CME Solar Sources

In this section we focus on the solar sources of cloud *a* and cloud *b* in ICME A and ICME B, respectively. Remarkably, even though the same magnetic field configuration was the source of the associated flares in both cases, the plot of θ_{GSE} in Figure 3 indicates that these clouds have oppositely directed leading and trailing magnetic fields, southward followed by northward in the case of cloud *a* and northward followed by southward in the case of cloud *b*. The Dst index was higher for cloud *a* (Dst ≈ -370 nT) than cloud *b* (Dst ≈ -290 nT). We will look at these events to discuss possible differences in their sources that might account for the opposite magnetic field configurations.

5.1. The Source of ICME A and Related Events

5.1.1. Flare and Eruption on 6 November 2004

The large M9.3 flare on 6 November in AR10696 is composed of three main stages, as shown in Figure 1 in the GOES data. Although the TELs exist at this time the flare predominantly occurs within the AR for the first two stages. The first stage starts at 00:11 UT and peaks at 00:34 UT. The second stage peaks at 00:57 UT. The third stage, which peaks at 01:57 UT, has a long decay phase of approximately 4 hours. This last event involves a larger area than the first two events with three flare ribbons observed by EIT. Dimmings cover a large

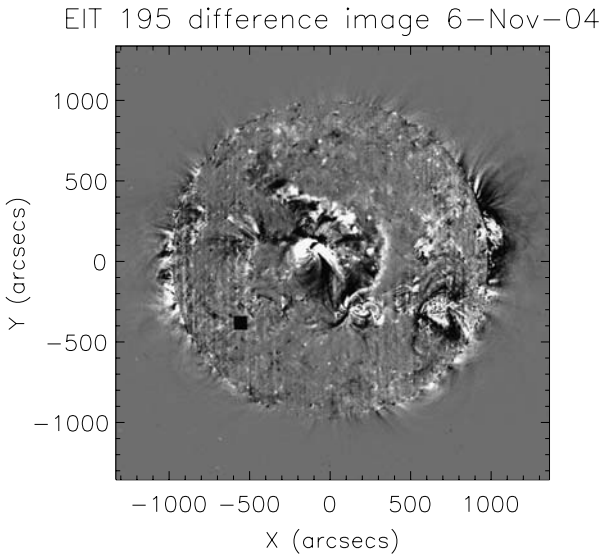

Figure 5 The EIT difference image (195 Å) produced using data at the start of the flare sequence on 5 November at 23:11 UT and on 6 November at 01:47 UT. The second image has been derotated. The main dimming region is encircled by a bright front.

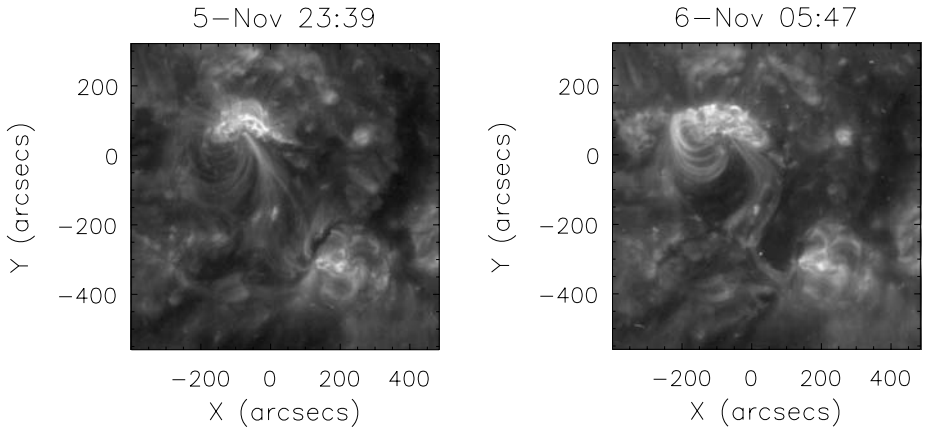

Figure 6 EIT (195 Å) images: The left panel shows the pre-flare morphology. AR10696 has a small coronal hole to the east and a more extended coronal hole to the west. The right panel shows the morphology at the end of the decay phase of the flare on 6 November. At this stage, it is particularly clear that there is a noticeable change in the TELs.

region that surrounds the western zone of the AR, as shown in Figure 5. There is a "coronal wave" seen in both the EIT and the Soft X-ray Imager (GOES-SXI). This wave does not traverse the whole solar disk but stops at the western coronal hole boundary (Figure 5), which subsequently brightens for around one hour. During this last stage the TELs appear bright and are seen to change (see Figure 6), but they do not erupt.

From the timing (see Section 4.1), there is little doubt that ICME A is the interplanetary counterpart of the CME that reached LASCO C2 on 6 November at 02:06 UT. We can see from Figure 2 that the AR has a positive northern magnetic field and a negative southern magnetic field, that is, a southward-oriented overlying arcade field. The ICME magnetic

field orientation is consistent with the magnetic orientation of the AR; furthermore, the direction of cloud *a* axis is consistent with the AR inversion line (see Section 5.1.2).

5.1.2. The Coronal Scenario of ICME A

During the CME on 6 November, magnetic loops (mainly the arcade overlying the erupting flux rope) in AR10696 expanded. This expansion led to magnetic interchange reconnection with open fields from the extended positive coronal hole to the west – southwest of AR10696 and formation of new connectivities, manifested by the appearance of new TELs in Figure 6. These newly brightened loops appear more S-shaped than prior to this flare/CME event. The interchange reconnection may have been driven from the coronal wave interaction with the coronal hole boundary, that is, the bright front appears when the expanding CME loops collide and reconnect with the open field lines at the coronal hole boundary in the same manner as proposed by Attrill *et al.* (2006) and Crooker and Webb (2006) for the 15 May 1997 CME event. Figure 7 shows a simplified cartoon of these changes in the magnetic configuration.

Although the cartoon in Figure 7 illustrates interchange reconnection between closed loops in AR10696 and open fields in a coronal hole, it seems unlikely that this process is responsible for the open fields in the resulting MC at 1 AU. Open fields in the interval labeled cloud *a* in Figure 3 are indicated in the top panel by the lack of field-aligned counter-streaming electron beams, which would signal fields connected to the solar source of these electrons at both ends, as seen within the trailing portion of ICME A. Instead the pitch-angle distributions in the cloud show peak flux only parallel to the magnetic field ($\approx 0°$), indicating open fields with positive polarity, *i.e.*, pointing away from the Sun.

Why the interchange reconnection illustrated in Figure 7 seems to be an unlikely means of opening the cloud fields becomes clear upon consideration of three-dimensional aspects

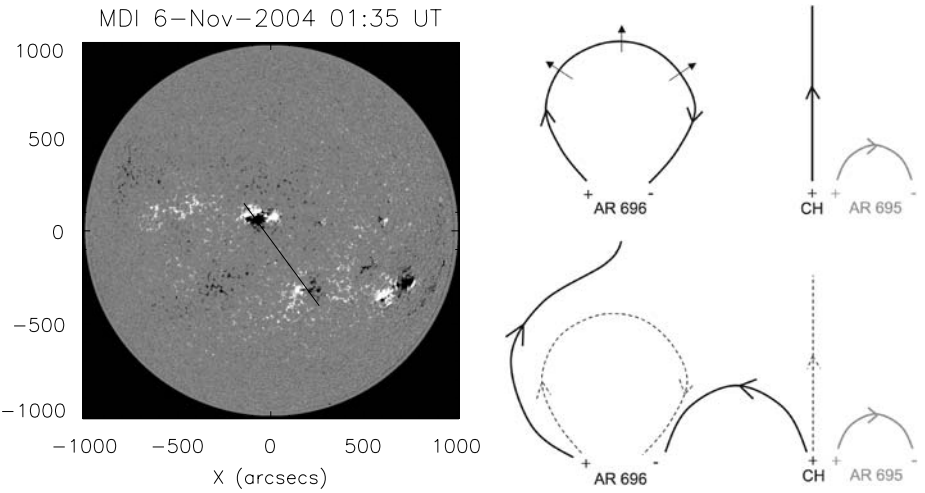

Figure 7 The figure to the left shows the MDI image with the orientation of the cartoon overlaid as a black solid line. The top right image illustrates the magnetic configuration during the flare on 6 November showing the expanding loops. This shows the connections before the event, *i.e.,* AR10696 and AR10695 and the coronal hole (CH) open lines. The lower right image illustrates the newly created connections by interchange reconnection between the expanding loops from AR10696 and the CH. The solid lines correspond to the new TELs and new open field lines; dashed lines correspond to the original configuration. Loops in AR10695 do not participate in this reconnection process.

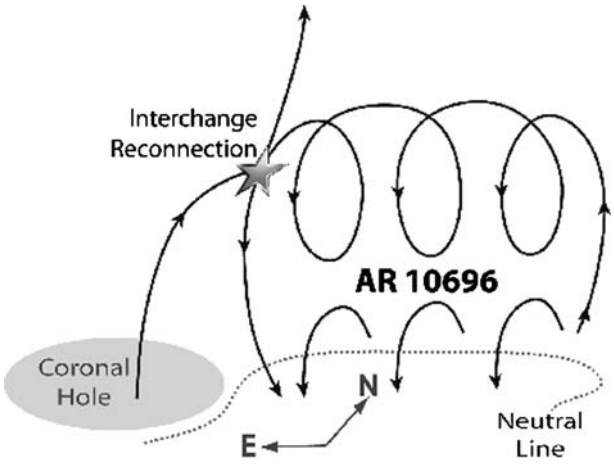

Figure 8 Schematic drawing of the magnetic development of cloud *a*. A closed coil in flux rope interchange reconnects at its end with open field line from the east coronal hole to form an open coil with positive polarity.

of the CME configuration, illustrated in Figure 8. Three AR10696 loops are shown in a view that is roughly orthogonal to the Figure 7 view. Above the loops is a coiled field representing the flux rope that becomes the MC. It is assumed that the flux rope is formed by reconnection of sheared rising loops, as in most CME models. The loops in Figure 8 are those returned to the Sun from the flux-rope formation process. They outline the bright arcade that comprises the flare associated with the reconnection. To disconnect from the Sun, interchange reconnection must occur not with rising loops, as in Figure 7, but with the flux rope. Moreover, to release the coiled portion of the field into the heliosphere as an open structure, interchange reconnection must occur in a specific leg of the coiled loop. For the case considered here, it must occur in the eastern leg to produce open coils with positive polarity. Thus, the open fields that participate in the interchange reconnection must be located near the east end of the coil. The most likely source there is a small coronal hole to the east of AR10696 and illustrated schematically in Figure 8.

Signatures of the required interchange reconnection in the coronal hole are apparent in the EIT images in Figure 6. The left image shows the hole as the dark region east of AR10696, and the right image shows it filled with bright spots. These "EIT crinkles" are thought to be the footpoints of the closed loops newly formed by interchange reconnection, as illustrated in Figure 8 (*e.g.*, Sterling and Moore, 2001; Crooker and Webb, 2006).

In addition, to illustrate the location of the interchange reconnection that opened its fields, Figure 8 also explains how the magnetic properties of cloud *a* match the expected configuration of a flux rope arising from AR10696. In particular, the leading fields in cloud *a* are southward (negative θ_{GSE} in Figure 3), as they must be if the rope was formed by reconnection of southward-pointing rising loops. The arcade loops in Figure 8 that return to the Sun and comprise the flare also point southward. In general, then, Figure 8 illustrates how flare loops serve as indicators of leading-field orientation in associated MCs. Further, the southward-leading fields in cloud *a* combined with its eastward axial field ($\phi_{\mathrm{GSE}} \approx 90°$) give a left-handed sense of twist, matching the sense of helicity buildup associated with the active region (see Longcope *et al.*, 2007).

The magnetic properties of cloud *a* have been quantified by fitting the observations to the classical linear force-free field model by Lundquist (1950). Here we use the simpler minimum variance method, which gives similar results. Identification of the leading cloud boundary was complicated because of the presence of what appears to be a reverse shock at 04:17 UT on 8 November, where Figure 3 shows a rise in V_{p} and a drop in B. A break in the

latitude angle θ_{GSE} at the leading boundary of ICME A itself, however, marked by a drop in T_p at 22:30 UT on 7 November, suggests a coincident cloud boundary there. With this leading boundary and a trailing boundary at 17:00 UT on 8 November, where θ_{GSE} ceases its smooth rotation, the model yields a typical diameter of 0.30 AU and axis-orientation parameters in GSE coordinates of latitude $-16°$ and longitude 86°. These values were obtained with a minimum variance scheme (Bothmer and Rust, 1997) after normalizing the field to eliminate the large variance in field magnitude owing not only to the presence of the reverse shock but also to the strong decline caused by expansion. The latitude angle indicates that the cloud axis lay nearly parallel to the ecliptic plane, as would be expected from the east – west orientation of the neutral line running through AR10696, and the longitude angle indicates that the spacecraft encountered the flux rope loop nearly head-on.

5.2. The Source of ICME B and Related Events

5.2.1. Flare and Eruptions on 7 November

The largest flare in the series from AR10696 occurred on 7 November, reaching X2.0 class, as seen in Figure 1. It is also a multiple event. The GOES lightcurve rises steeply at ≈15:50 and has two clear peaks at ≈16:00 UT and ≈16:35 UT. The EIT difference images initially show an intense brightening of the core AR loops, which corresponds to the steep rise in GOES. This intense brightening is followed by large-scale dimmings (Figure 9). The bulk of the dimming (the deepest one) seems to be due to the eruption of the TE filament (see Figure 10), as shown in the right panel of Figure 9. This eruption, together with a large two-ribbon flare in the AR, accounts for the first peak in GOES. Figure 10 shows EIT images corresponding to this event. The left top panel shows the formation of two flare ribbons at both sides of the eruptive filament, which is seen in Hα in the bottom right panel prior to its eruption. The global magnetic field configuration is depicted in the MDI map on the bottom left panel. The formation of the post-flare loops in the AR is seen in the top right panel of Figure 10 and also in the EIT difference image of Figure 9 (right panel). The orientation of the post-flare loops relative to the magnetic inversion line clearly shows the shear of the

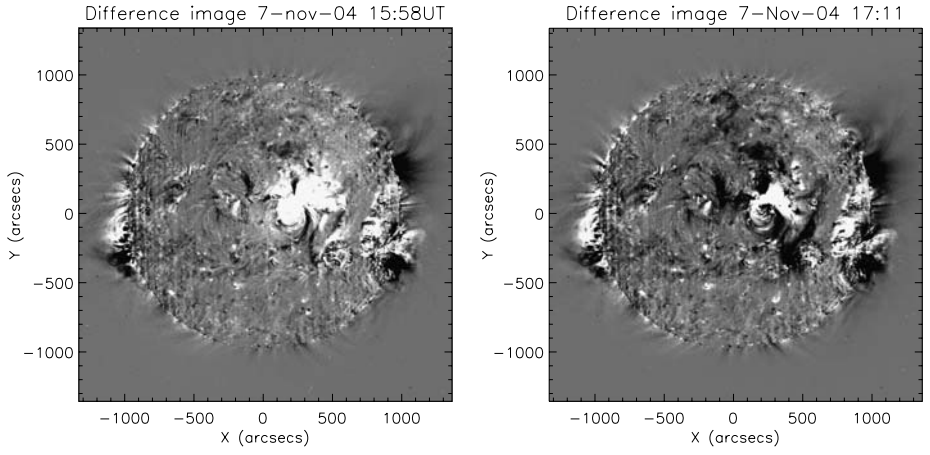

Figure 9 Left: EIT base difference image during the rise phase of the 7 November flare. The active region has increased in brightness. Right: EIT difference image following the TE filament eruption. The large dimming areas can be clearly seen. For both difference images, the subtracted image was a pre-flare image.

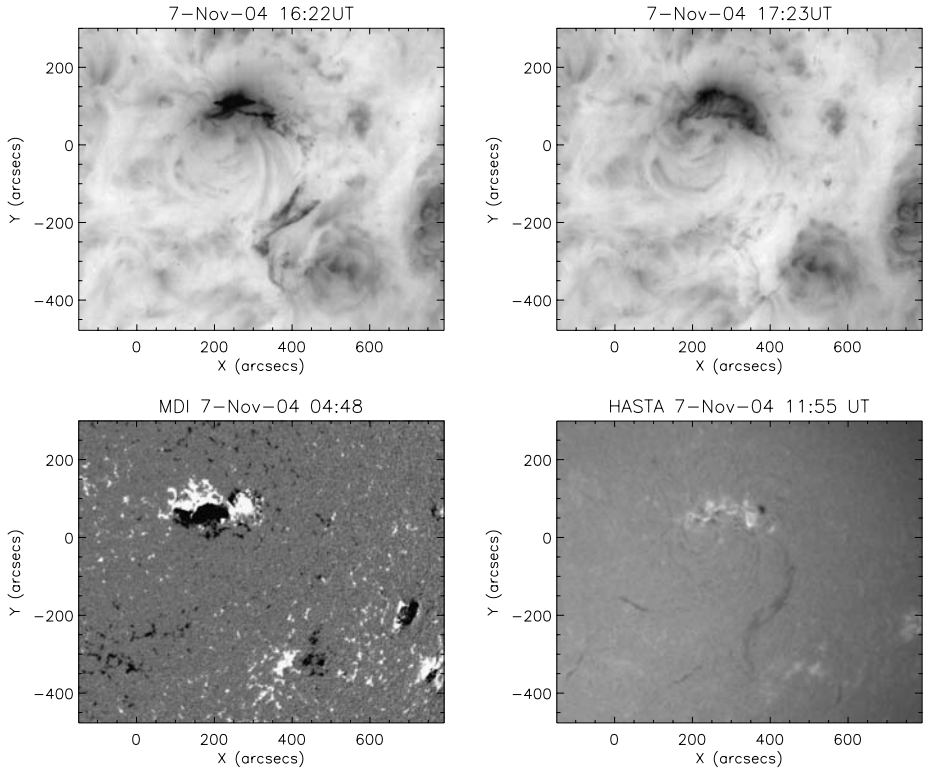

Figure 10 Images showing the evolution of the 7 November event. Top left: Evidence of the TE filament erupting in EIT. Top right: The post-flare loops having formed in AR10696 (also in EIT). Bottom left: The MDI image. Bottom right: The Hα image showing the TE filament before eruption (from HASTA).

loops. The filament and TEL eruption was most likely induced by an instability associated with the event, which started a few minutes before a visible excitation of the filament was seen in Hα. By 18:43 UT the TEL system reformed and brightened by 18:43 UT. The CME observed in LASCO C2 on 7 November at 16:54 UT is associated with this multiple flare involving AR10696 and the erupting filament to the southwest.

5.2.2. Clues from Interplanetary Scintillation Data

To gain some insight on the interplanetary consequences of the complex flare and eruptions, heliospheric density and speed patterns were reconstructed from interplanetary scintillation (IPS) measurements. Figure 11 shows a 3D tomographic reconstruction as a remote observer would view the heliosphere in electron density (left) and speed (right) from east of the Sun – Earth line and a few degrees above the ecliptic plane. The reconstruction is derived using the Solar-Terrestrial Environment Laboratory (STELab, Japan) IPS data on 9 November 2004 at 03:00 UT out to 1.5 AU. The Sun is at the center of the coordinate system and the Earth is a blue dot on its orbit depicted as a purple ellipse.

Our 3D analysis is a weighted 3D solar wind reconstruction technique that merges approximately one week of Japanese STELab IPS scintillation-level and velocity data to provide a global reconstruction of the solar wind density and velocity at the time indicated. The scintillation measurements can be made in weak scattering at 327 MHz (the STELab IPS

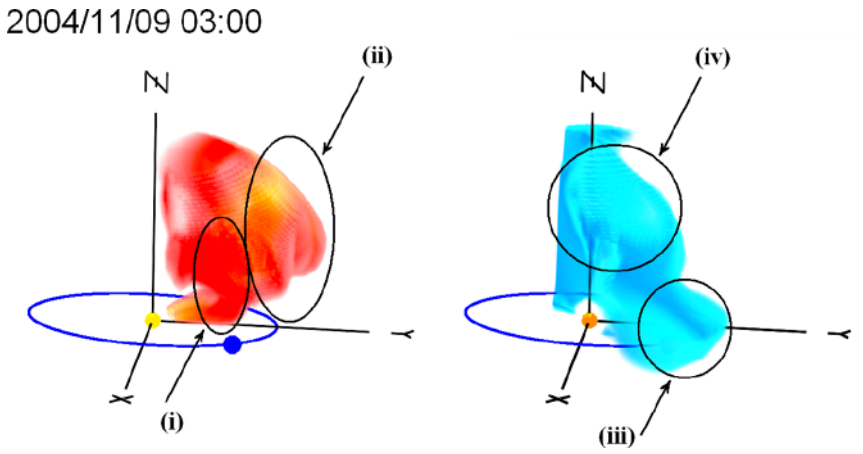

Figure 11 3D tomographic reconstruction as a remote observer would view the heliosphere in electron density (left) and speed (right) from east of the Sun – Earth line and a few degrees above the ecliptic plane, as derived from STELab (Japan) IPS data on 9 November 2004 at 03:00 UT out to 1.5 AU. For the reconstructed heliospheric structures, the brighter the color, the greater the value for both the electron density (between 15 and 50 cm^{-3}) and speed (from 900 $km\,s^{-1}$). Everything in the southern hemisphere, in the foreground, and behind the Sun (away from the Earth), has been removed for clarity and to limit obscuration of the points of interest. In this figure, (i) is the 7 November event as seen in LASCO C2 at 16:54 UT, (ii) is the combination of the two 6 November events as seen in LASCO C2 at 01:31 UT and 02:06 UT, (iii) shows high velocity engulfing the Earth, which lags the 6 November events but precedes the 7 November event and is comparable in velocity to that detected by LASCO C2 for the 7 November event, and (iv) shows high-speed solar wind going mainly northward, consistent with the speeds of (iii).

radio frequency) to approximately 11.5 degrees elongation from the Sun as viewed from Earth. No radio sources are used in the reconstructions at nearer elongations from the Sun in the UCSD analyses. The reconstructed solar wind analyses are extrapolated below this elongation by using the assumptions inherent in the solar wind model. In the case of Figure 11, this is close to the inner boundary that is reconstructed.

What appears to be unique to the 7 November events ((i) in Figure 11), in particular, compared to the 6 November events ((ii) in Figure 11), is a tongue of high-speed plasma that separates from the bulk of outward-moving plasma and seemingly spreads out in the equatorial plane and northward. It is possible that this tongue was driven by the eruption from the TE filament and loops, while the material from the core of the active region went primarily northward, merging with the material from the 4 and 6 November events. The videos associated with this figure, and included in the electronic version of this paper (density.gif and velocity.gif), extend out to 3 AU; they show an electron density range between 20 and 50 cm^{-3} (to allow ease of viewing the very dense portions in a moving image) and speed from 900 $km\,s^{-1}$ and above in a wider color scale for higher speeds. This range of volume elements and colors are depicted in the inserted histograms. The sequence of images extends from 8 November 2004 at 03:00 UT to 12 November 2004 at 21:00 UT.

This two-part interplanetary view helps to explain the ICME B information in Table 1. It is consistent with the passage of two shocks (4 and 5). Shock 4 marked a strong shift in flow direction, consistent with a driver north of the spacecraft, from the core of the AR; shock 5 was encountered head-on, consistent with the tongue of high-speed flow from the TE filament – loop system. Moreover, in the two-part view, the high northward speed (1759 $km\,s^{-1}$) of the CME observed by LASCO in C2 on 7 November at 16:54 UT would correspond to

the material erupting from the core, and use of that speed to predict ICME arrival at Earth from the formula of Gopalswamy *et al.* (2001) would naturally produce a time that is too early, as indicated in Table 1. The Cliver, Feynman, and Garrett (1990) formula implies that the earthward speed of the northward-moving CME material was only $\approx$1100 km s^{-1}.

5.2.3. The Coronal Scenario of ICME B

As noted in Section 4, cloud *b* in ICME B had northward leading fields, in contrast to the southward leading fields of cloud *a* in ICME A. Figure 12 illustrates the configurations of both along with those of their presumed solar sources. Both clouds had left-handed twist, which means that their axial fields as well as their leading and trailing fields were opposite to each other. For cloud *b*, the minimum variance model yields a diameter of 0.24 AU, similar to that of cloud *a* (0.30 AU), and axis orientation parameters in GSE coordinates of latitude -20° and longitude 276°. Thus, the axes of both clouds lay roughly perpendicular to the Earth – Sun line, and their model tilts relative to the ecliptic plane are as drawn in Figure 12.

Although the magnetic properties of cloud *a* match the expected configuration of a flux rope arising from AR10696, as illustrated in both the solar view in Figure 8 and the interplanetary extension in Figure 12, the opposite magnetic properties of cloud *b* seem to require a different source. The large-scale magnetic interactions during the 7 November event were different from those of the previous day; in this case both the AR and the TEL system and filament erupted.

Our proposed source for cloud *a*, AR10696, has been proposed as the source of cloud *b* by Longcope *et al.* (2007), based upon an innovative model that uses measured changes in magnetic flux as input. However, if we adhere to the standard view that the leading cloud fields match the bright arcade fields of the flare, as for cloud *a*, the same source would require that cloud *b* had rotated by 160° during the eruption and/or on its journey between the Sun and 1 AU. A possible alternative source, in the context of the standard view, is the TEL system joining AR10695 to AR10696, as sketched in the right panel of Figure 12, since their northward fields roughly match the leading cloud fields. However, in the case of a disappearing filament, like the TE filament, one also expects a match between the filament and cloud axes (*e.g.*, Marubashi, 1986), and these differ by 67°, as drawn.

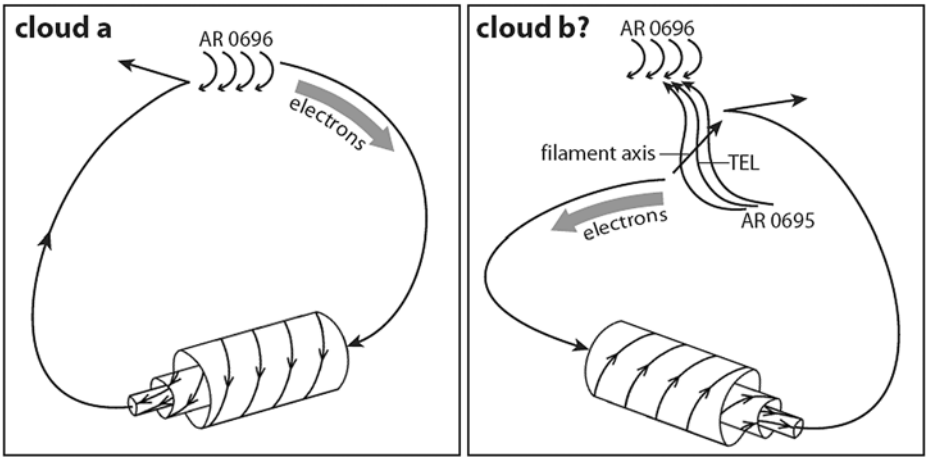

Figure 12 Schematic drawings of the magnetic configurations of magnetic clouds *a* (7 – 8 November 2004) and *b* (9 – 10 November 2004) and their presumed solar source regions.

We note that a near match is obtained by using the axis orientation of the first of two successive flux ropes fit to cloud *b* by R.P. Lepping (http://lepmfi.gsfc.nasa.gov/mfi). Alternatively, the second flux rope has a leading southward field that could provide the match to the associated arcade, as for cloud *a*. Dasso *et al.* (2007), however, reject the two-rope solution based upon advanced modeling of this event, and we adopt their position and continue with our discussion of the single-rope solution. Another problem with its axis orientation is that the sense of rotation from the filament to the cloud is clockwise, not counterclockwise as one might expect from the development of a kink instability in a region of left-handed helicity (Green *et al.*, 2007). Of course the kink instability may not have played a role in this case, especially away from the strong fields of the active regions, and it is not clear if observed rotations of filaments (*e.g.*, Williams *et al.*, 2005) control the orientation of the much larger flux rope that comprises the cloud. It is possible that the rotation was caused by the large-scale dynamics and interaction between the presumed two parts of the ejection, as discussed in Section 5.2.2. We will discuss these alternatives further in Section 6.

Figure 12 also shows the direction of the observed suprathermal electron beams in cloud *a* and cloud *b*. In both cases, the pitch-angle distributions in the top panel of Figure 3 indicate that they were parallel to the magnetic field, implying that interchange reconnection had released field lines in the negative leg. In case of cloud *a* this interchange reconnection could have occurred with the small positive polarity coronal hole to the east of AR10696, as discussed in Section 5.1.2 for cloud *a*. In the case of cloud *b*, the source of open fields for release of the negative leg should have been to the west, but its location is not apparent in the EIT images. Some interchange reconnection to the east may have released field lines in the positive leg, as well, creating coils completely disconnected from the Sun. This possibility is suggested by what appears to be sporadic dropouts of the suprathermal beam in the pitch-angle distributions, beginning around 00:00 UT on 10 November.

6. Discussion

We have analyzed the chain of events, from Sun to Earth, that gives rise to the two largest geomagnetic storms associated with the solar activity period on November 2004. We have found that the same global magnetic field configuration can be the source of MCs with oppositely directed magnetic fields. Furthermore, the two geomagnetic storms caused by the arrival of these clouds at Earth have different intensity; the one associated with the cloud with southward leading field was more intense than the one linked to the cloud with northward leading field. Our results agree with those of Liu, Webb, and Zhao (2006).

From our analysis, it is clear that the complex flare and eruption occurring in AR10696 on 6 November 2004 was the source of the ICME/MC observed from 7 November to 8 November by ACE (ICME A/cloud *a*). This is supported by the agreement between cloud *a* southward leading fields and the magnetic field orientation of the flare loops (positive footpoints in the north and negative footpoints in the south, cloud axis nearly parallel to the ecliptic plane and main AR polarity inversion line running east – west, and negative magnetic helicity, in both the AR and the cloud).

For the ICME/MC observed by ACE from 9 to 10 November (ICME B/cloud *b*), our combined analysis of solar and interplanetary data leads us to consider two alternative sources. Cloud *b* had leading northward field and negative magnetic helicity, and its axis lay almost on the ecliptic plane. During the complex flare and eruption on 7 November 2005, both AR10696 magnetic field and a system of TE loops and filament erupted.

Longcope *et al.* (2007) have proposed that AR10696 was the source of cloud *b*. If this is the case, the flux tube forming cloud *b* would need to rotate $\approx 160^\circ$ counterclockwise from

Sun to Earth, considering the standard view in which the field orientation in the bright flaring loops should match the direction of the cloud leading field. Is such a large rotation possible? AR10696 had a high magnetic helicity content, as discussed by Longcope *et al.* (2007), and hence highly twisted flux ropes could have been present in the region. In a later event from the same AR (on 10 November), Williams *et al.* (2005) showed that an erupting filament/flux rope rotated 90° within the *Transition Region and Coronal Explorer* field of view. However, in this case it was not known what the rotation would have been by the time the flux tube reached 1 AU, since the eruption was at the limb and it did not reach Earth. Török's (2006, private communication) simulations of erupting flux ropes undergoing kink instability show that rotations as high as half a turn (180°) are possible in the low corona. The sense of rotation is counterclockwise for flux tubes having negative helicity. However, an important question is why the eruptions would be so drastically different on two consecutive days, producing no rotation of the erupting filament on 6 November and a large rotation on 7 November. There are two reasons why such a large rotation may be possible: *i*) Helicity is increased owing to continuing twisted flux emergence in the 40 hours between the two events (see Longcope *et al.*, 2007). *ii*) There was no removal of helicity between the two events via CMEs. Démoulin *et al.* (2002) and Green *et al.* (2002) have proposed that CMEs deplete the helicity in the AR. Mandrini *et al.* (2005) and Luoni *et al.* (2005) have provided observational evidence for this. As can be seen from Figure 1, there were no major eruptions for about 40 hours after the event on 6 November.

An alternative source for ICME B/cloud *b* is the eruption of the TE loop system (joining AR10696 and AR10695) and TE filament, as proposed in this paper. The northward direction of the leading magnetic field in cloud *b* matches the magnetic field direction in the TELs. However, the axis of cloud *b* differs from the filament direction by 67°. This angular difference cannot be explained by the onset of a kink instability during eruption in the low corona, since the sense of rotation from the solar source to cloud *b* is clockwise. As stated in Section 5.2.3, it may also happen that the kink instability does not play a role far away from the strong fields of the AR; then, the rotation could be caused by the large-scale dynamics and interaction between the presumed two parts of the ejection.

One may also question that both the flux and helicity are likely to be too low in the TE quiet-Sun filament and surrounding magnetic field to match the high values found in cloud *b*. The magnetic flux and helicity in MCs can be quantified from observations by using several models (see, *e.g.*, Dasso *et al.*, 2003). The magnetic flux in cloud *b* is $\approx 4.7 \times 10^{21}$ Mx for a cloud length of 1 AU, but its magnetic helicity is -5.0×10^{42} Mx^2 (see Longcope *et al.*, 2007). We have estimated the photospheric flux in the field surrounding the TE filament and extending as far as the two flare ribbons observed in EIT after the filament eruption; this flux value is $(1.0-2.0) \times 10^{21}$ Mx (the average of the positive plus the absolute value of negative fluxes above the MDI noise level of 9 G). This estimation excludes the flux that could be added through ongoing tether-cutting reconnection to the erupting flux tube and hence is a lower bound estimate. It is surprising that both magnetic fluxes (in cloud *b* and in magnetic field surrounding the TE filament) agree within an order of magnitude. Since magnetic helicity is proportional to magnetic flux to the second power it may not be impossible for the TE filament and surrounding fields to have a large helicity content. Unfortunately, we have no means of estimating the helicity in this region.

This leaves us with ambiguity for the source of cloud *b* that is difficult to resolve with the current data sets.

7. Conclusion

We have studied two magnetic clouds that originated from the same flaring magnetic configuration and found that the associated magnetic clouds had opposite magnetic orientations. The first magnetic cloud matched the configuration in the flaring active region, but the second cloud source was ambiguous. The latter could be associated with a large rotation of the erupting flux tube coming from the active region or with a trans-equatorial filament eruption.

This work has emphasized strongly the need to link closely the solar and in situ observations of the magnetic structures seen if we are to understand the Sun – Earth system and ultimately be able to determine geoeffectiveness. In our study dramatic changes occurred in the flaring active region between the start of ICME A and ICME B that would have been difficult to predict. Although statistical studies are useful for a broad understanding, in this example they would not have helped us to understand the observed cloud orientation.

Future observations using *Hinode*, along with the 3D view of CMEs from STEREO should progress understanding of this problem further. *Hinode* will be able to determine the detailed morphology, including twist of the solar source. STEREO will be able to track the 3D view as ICMEs travel toward Earth.

Acknowledgements L.K.H. acknowledges the Leverhulme Trust for the award of a Philip Leverhulme prize that enabled the Sun – Earth workshop to take place. The authors thank the SOHO/EIT and SOHO/MDI consortia for their data. SOHO is a project of international cooperation between ESA and NASA. This study is partially based on data obtained at OAFA (El Leoncito, San Juan, Argentina) in the framework of the German – Argentinean HASTA/MICA Project, a collaboration of MPE, IAFE, OAFA, and MPAe. CHM and SD acknowledge support from Argentinean Grant Nos. UBACyT X329 (UBA), PICTs 03-12187 and 03-14163 (ANPCyT), and PIP 6220 (CONICET). This research has made use of ACE data. LvDG acknowledges the Hungarian Government Research Grant No. OTKA 048961. NUC acknowledges U.S. National Science Foundation Grant No. ATM-0553397. The authors thank Pascal Démoulin for enlightening discussions.

References

Attrill, G.D.R., Nakwacki, M.S., Harra, L.K., van Driel-Gesztelyi, L., Mandrini, C.H., Dasso, S., Wang, J.: 2006, *Solar Phys.* **238**, 117.

Bothmer, V., Rust, D.M.: 1997. In: Crooker, N., Joselyn, J.A., Feynman, J. (eds.) *Coronal Mass Ejections*, *Geophys. Monograph* **99**, American Geophysical Union, Washington, 139.

Burlaga, L.F.: 1995, *Interplanetary Magnetohydrodynamics*, Oxford University Press, New York.

Chertok, I.M.: 2006, *Astron. Rep.* **83**, 76.

Cliver, E.W., Feynman, J., Garrett, H.B.: 1990, *J. Geophys. Res.* **95**, 17103.

Crooker, N.U., McAllister, A.H., Fitzenreiter, R.J., Linker, J.A., Larson, D.E., Lepping, R.P., Szabo, A., Steinberg, J.T., Lazarus, A.J., Mikic, Z., Lin, R.P.: 1998, *J. Geophys. Res.* **103**, 26859.

Crooker, N.U., Webb, D.F.: 2006, *J. Geophys. Res.* **111**, A08108.

Dasso, S., Mandrini, C., Démoulin, P., Luoni, M.L.: 2003, *J. Geophys. Res.* **455**, 349.

Dasso, S., Nakwacki, M.S., Démoulin, P., Mandrini, C.: 2007, *Solar Phys.*, doi: 10.1007/s11207-007-9034-2.

Delaboudinière, J.-P., Artzner, G.E., Brunaud, J., Gabriel, A.H., Hochedez, J.F., Millier, F., *et al.*: 1995, *Solar Phys.* **162**, 291.

Démoulin, P., Mandrini, C.H., van Driel-Gesztelyi, L., Thompson, B., Plunkett, S., Kővári, Z., Aulanier, G., Young, A.: 2002, *Astron. Astrophys.* **382**, 650.

Elliott, H.A., McComas, D.J., Schwadron, N.A., Gosling, J.T., Skoug, R.M., Gloeckler, G., Zurbuchen, T.H.: 2005, *J. Geophys. Res.* **110**, A04103.

Fazakerley, A.N., Harra, L.K., Culhane, J.L., van Driel-Gesztelyi, L., Lucek, E., Matthews, S.A., Owen, C., Mazalle, C., Balogh, A., Rème, H.: 2005, *Geophys. Res. Lett.* **32**, L13105.

Fernández Borda, R.A., Mininni, P.D., Mandrini, C.H., Gómez, D.O., Bauer, O.H., Rovira, M.G.: 2002, *Solar Phys.* **206**, 347.

Fry, C.D., Dryer, M., Smith, Z., Sun, W., Deehr, C.S., Akasofu, S.-I.: 2003, *J. Geophys. Res.* **108**(A2), 1070.

Gopalswamy, N., Lara, A., Yashiro, S., Kaiser, M.L., Howard, R.A.: 2001, *J. Geophys. Res.* **106**, 29207.

Green, L.M., López Fuentes, M.C., Mandrini, C.H., Démoulin, P., van Driel-Gesztelyi, L., Culhane, J.L.: 2002, *Solar Phys.* **208**, 43.
Green, L.M., Török, T., Kliem, B., Attrill, G.D.R., van Driel-Gesztelyi, L.: 2007, *Solar Phys.*, submitted.
Kang, S.-M., Moon, Y.-J., Cho, K.-S., Kim, Y.-H., Park, Y.-D., Baek, J.-H., Chang, H.-Y.: 2006, *J. Geophys. Res.* **111**, A05102.
Khan, J.I., Hudson, H.S.: 2000, *Geophys. Res. Lett.* **27**, 1083.
Liu, Y., Webb, D.F., Zhao, X.P.: 2006, *Astrophys. J.* **646**, 1335.
Longcope, D., Beveridge, C., Qiu, J., Ravindra, B., Barnes, G., Dasso, S.: 2007, *Solar Phys.*, doi: 10.1007/s11207-007-0330-7.
Lundquist, S.: 1950, *Ark. Fys.* **2**, 361.
Luoni, M.L., Mandrini, C.H., Dasso, S., van Driel-Gesztelyi, L., Démoulin, P.: 2005, *J. Atmos. Solar-Terr. Phys.* **67**, 1734.
Mandrini, C.H., Pohjolainen, S., Dasso, S., Green, L.M., Démoulin, P., van Driel-Gesztelyi, L., Copperwheat, C., Foley, C.: 2005, *Astron. Astrophys.* **434**, 725.
Manoharan, P.K.: 2006, *Solar Phys.* **235**, 345.
Marubashi, K.: 1986, *Adv. Space Res.* **6**, 335.
McAllister, A.H., Martin, S.F., Crooker, N.U., Lepping, R.P., Fitzenreiter, R.J.: 2001, *J. Geophys. Res.* **106**, 29185.
McComas, D.J., Bame, S.J., Barker, P., Feldman, W.C., Phillips, J.L., Riley, P., Griffee, J.W.: 1998, *Space Sci. Rev.* **86**, 563.
Pevtsov, A., Canfield, R.C.: 2001, *J. Geophys. Res.* **106**, 25191.
Pohjolainen, S., van Driel-Gesztelyi, L., Culhane, J.L., Manoharan, P.K., Elliott, H.: 2007, *Solar Phys.*, doi: 10.1007/s11207-007-9006-6.
Scherrer, P.H., Bogart, R.S., Bush, R.I., *et al.*: 1995, *Solar Phys.* **162**, 129.
Schwenn, R., Dal Lago, A., Huttunen, E., Gonzalez, W.D.: 2005, *Ann. Geophys.* **23**, 1033.
Smith, C.W., L'Heureux, J., Ness, N.F., Acua, M.H., Burlaga, L.F., Scheifele, J.: 1998, *Space Sci. Rev.* **86**, 613.
Sterling, A.C., Moore, R.L.: 2001, *J. Geophys. Res.* **106**, 25227.
Srivastava, N., Venkatakrishnan, P.: 2004, *J. Geophys. Res.* **109**, A10103.
Stone, E.C., Frandsen, A.M., Mewaldt, R.A., Christian, E.R., Margolies, D., Ormes, J.F., Snow, F.: 1998, *Space Sci. Rev.* **86**, 1.
Vilmer, N., Pick, M., Schwenn, R., Ballatore, P., Villain, J.P.: 2003, *Ann. Geophys.* **21**, 847.
Vrsnak, B., Gopalswamy, N.: 2003, *J. Geophys. Res.* **107**(A2), 1019.
Wang, J.-X., *et al.*: 2007, *Solar Phys.*, accepted.
Wang, J.-X., Zhou, G.-P., Wen, Y.-Y., Zhang, Y.-Z., Wang, H.-N., Deng, Y.-Y., Zhang, J., Harra, L.K.: 2006a, *Chin. J. Astron. Astrophys.* **6**, 247.
Wang, Y., Xue, X., Shen, C., Ye, P., Wang, S., Zhang, J.: 2006b, *Astrophys. J.* **646**, 625.
Webb, D.F., Cliver, E.W., Crooker, N.U., St Cry, O.C., Thompson, B.J.: 2000, *J. Geophys. Res.* **105**, 7491.
Williams, D.R., Török, T., Démoulin, P., van Driel-Gesztelyi, L., Kliem, B.: 2005, *Astrophys. J.* **628**, L163.
Yashiro, S., Gopalswamy, N., Akiyama, S., Michalek, G., Howard, R.A.: 2005, *J. Geophys. Res.* **110**, A12, S05
Zhou, G.-P., Wang, J.-X., Zhang, J.: 2006, *Astron. Astrophys.* **445**, 1133.